Double Perovskite Heterostructures: Magnetism, Chern Bands, and Chern Insulators

Ashley M. Cook[1] and Arun Paramekanti[1,2]
[1]Department of Physics, University of Toronto, Toronto, Ontario M5S 1A7, Canada
[2]Canadian Institute for Advanced Research, Toronto, Ontario M5G 1Z8, Canada
(Received 1 March 2014; published 13 August 2014)

Experiments demonstrating the controlled growth of oxide heterostructures have raised the prospect of realizing topologically nontrivial states of correlated electrons in low dimensions. Here, we study heterostructures consisting of {111} bilayers of double perovskites separated by inert band insulators. In bulk, these double perovskites have well-defined local moments interacting with itinerant electrons leading to high temperature ferromagnetism. Incorporating spin-orbit coupling in the two-dimensional honeycomb geometry of a {111} bilayer, we find a rich phase diagram with tunable ferromagnetic order, topological Chern bands, and a $C = \pm 2$ Chern insulator regime. Our results are of broad relevance to oxide materials such as Sr_2FeMoO_6, Ba_2FeReO_6, and Sr_2CrWO_6.

DOI: 10.1103/PhysRevLett.113.077203 PACS numbers: 75.47.Lx, 71.10.Fd, 73.43.−f, 74.78.Fk

Quantum anomalous Hall (QAH) insulators or Chern insulators (CIs) are remarkable topological phases that exhibit a quantized Hall effect even in the absence of a net magnetic field [1]. Proposals for candidate materials to realize these phases include weakly correlated systems such as doped topological insulator (TI) films [2] or TI interfaces [3], topological crystalline insulators [4], metallic chiral magnets [5,6], silicene [7,8], and graphene [9–13]. Recent experiments on $(Bi, Sb)_2Te_3$ TI films doped with magnetic Cr atoms have reported the first observation of the QAH effect [14] at temperatures $T \lesssim 0.5$ K, although issues related to bulk conduction [15] and Cr doping inhomogeneities [16] remain to be clarified.

A parallel significant development in recent years has been the experimental breakthrough in growing transition metal oxide (TMO) heterostructures [17–19]. This has motivated a significant effort towards understanding the interplay of strong electron correlations, quantum confinement, and spin-orbit coupling (SOC) in driving topological states of electrons in cubic perovskites ABO_3, in pyrochlores $A_2B_2O_7$, or at oxide interfaces [20–33]. Realizing CIs in TMOs would be particularly useful since one expects the associated energy gaps and temperature scales to observe this phenomena to be significantly higher. It would also set the stage for realizing exotic correlation-driven fractional CIs [34–37].

The challenge in stabilizing CIs in simple TMOs stems from a delicate balance of energy scales. (i) Strong electronic correlations are crucial to drive magnetic order of the transition metal (TM) ion, thus breaking time-reversal symmetry, yet correlations should not be so strong as to cause Mott localization. (ii) SOC on the TM ion needs to be significant to convert the magnetic exchange field into an orbital magnetic field for producing a QAH effect, yet outer shell electrons in heavy elements with strong SOC are also typically weakly correlated and nonmagnetic.

In this Letter, we propose that ordered double perovskites (DPs) [38], oxides with the chemical formula $A_2BB'O_6$, having transition metal ions B and B′ residing on the two sublattices of a 3D cubic lattice as shown in Fig. 1(a), can circumvent these difficulties. For suitable choices of B, B′ ions, such that B is a $3d$ element with strong electronic correlations driving local moment magnetism, while B′ is a $4d$ or $5d$ element that has itinerant electrons with strong SOC, one obtains both key ingredients for realizing a CI. Thus, we propose metallic $3d/4d$ or $3d/5d$ DPs with high magnetic transition temperatures in the bulk to be promising platforms for realizing CIs in a layered geometry.

We bolster this proposal by studying topological phases emerging in {111} bilayers of DPs sandwiched between inert band insulating oxides, forming a heterostructure. The motivation for this work stems from recent experiments on $(LaNiO_3)_m$-$(LaMnO_3)_n$ oxide superlattices grown along the {111} direction [39] for various values of m, n. The (1, 1) superlattice, with alternately stacked triangular layers

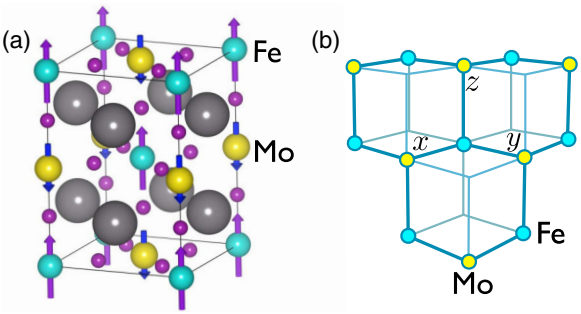

FIG. 1 (color online). (a) Crystal structure of the double perovskite Sr_2FeMoO_6. Arrows depict ferrimagnetic configuration of spins on the Fe and Mo sites in bulk Sr_2FeMoO_6. (b) {111} view of a bilayer, showing buckled honeycomb lattice with Fe and Mo ions on the two sublattices.

of Ni ions and Mn ions, corresponds to the DP La_2NiMnO_6, a candidate multiferroic DP [41]. Similarly, La_2FeCrO_6 has been grown artificially by alternately stacking stoichiometric $LaFeO_3$ and $LaCrO_3$ monolayers on $\{111\}$ oriented SrTiO3 substrate [40]. Here, we present our results for a Sr_2FeMoO_6 (SFMO) bilayer, as a prototypical example of a DP with high-T_c metallic ferromagnetism [42–48]. Preliminary results [49] suggest that a similar physics is to be found in other materials in this family, including Ba_2FeReO_6 [50,51] and Sr_2CrWO_6 [52].

As shown in Fig. 1(b), a $\{111\}$ DP bilayer of SFMO has Fe and Mo on the two sublattices of a (buckled) honeycomb lattice. The system consists of spin-orbit coupled t_{2g} electrons on the triangular lattice formed by Mo, coupled to local moments on the triangular Fe lattice. Our central result is the emergence, in this system, of $C = \pm 1$, ± 2 Chern bands, and CIs with a QAH effect, driven by spontaneous ferromagnetism of Fe moments.

Our study of the magnetism and electronic states in the SFMO bilayer reveals the following. Among a large variety of magnetically ordered or disordered states we have examined, the ferromagnetically ordered state of the Fe moments has the lowest energy. This is consistent with experimental [42] and theoretical [47] results on bulk SFMO. The interplay of SOC, interorbital hybridization, and a symmetry-allowed trigonal distortion leads to different orientations of the ferromagnetic order, with distinct electronic properties. For the $\{1\bar{1}0\}$ orientation of magnetic order, we find electronic bands with Chern numbers $C = \pm 1$. For magnetic order along the $\{111\}$ direction, with Fe moments perpendicular to the bilayer, we find that the Mo t_{2g} electrons form bands with Chern numbers $C = \pm 2$; an effective two-band triangular lattice model of Zeeman-split $j = 3/2$ states correctly captures the emergence of this nontrivial band topology. These bands have a direct gap, but typically overlap in energy leading to a Chern metal. A symmetry-allowed trigonal distortion stabilizes a regime of a CI with $C = \pm 2$, i.e., a QAH insulator with a pair of chiral edge modes, having a gap ~75 K.

Model.—In SFMO, strong Hund's coupling on Fe^{3+} locks the $3d^5$ electrons into a $S_F = 5/2$ local moment, which we treat as a classical spin. The $4d^1$ electron on Mo^{5+} hops on or off Fe, subject to a charge-transfer energy Δ. Pauli exclusion on Fe forces the spin of the arriving electron to be antiparallel to the underlying Fe moment. Kinetic energy lowering then favors ferromagnetic order of the Fe moments in bulk SFMO [43–47]. Similar physics is found in Sr_2CrWO_6 [52], with a $S = 3/2$ moment on Cr^{3+} and an itinerant $5d^1$ electron on W, as well as Ba_2FeReO_6 [50,51] with a $S = 5/2$ moment on Fe and itinerant $5d^2$ electrons from Re. However, previous work has not considered the dual effect of quantum confinement and SOC in these oxides.

Here, we consider a $\{111\}$ bilayer of SFMO, which confines electrons to a honeycomb lattice (see Fig. 1). The Mo t_{2g} orbitals transform as $L = 1$ angular momentum states and experience local SOC, $-\lambda \vec{L} \cdot \vec{S}$, with $\lambda > 0$, leading to a low energy $j = 3/2$ quartet and a high energy $j = 1/2$ doublet. Finally, the reduced symmetry of the honeycomb bilayer in a thin film grown along $\{111\}$ permits a trigonal distortion [28] $H_{\rm tri} = \chi_{\rm tri}(\vec{L} \cdot \hat{n})^2$, where $\hat{n}$ is a unit vector perpendicular to the bilayer; $\chi_{\rm tri} > 0$ corresponds to compressing the Mo oxygen octahedral cage [53]. Incorporating these new ingredients, we arrive at the model Hamiltonian

$$H = \sum_{\langle ij\rangle,\ell,\sigma} [t_\ell^{ij} g_\sigma(j) d_{i\ell\sigma}^\dagger f_{j\ell} + \text{H.c.}] + \Delta \sum_{i\ell} f_{i\ell}^\dagger f_{i\ell} + H_{\rm tri} + \sum_{\langle\langle ij\rangle\rangle,\ell,\sigma} \eta_{\ell\ell'}^{ij} d_{i\ell\sigma}^\dagger d_{j\ell'\sigma} + i\frac{\lambda}{2} \sum_i \varepsilon_{\ell mn} \tau_{\sigma\sigma'}^n d_{i\ell\sigma}^\dagger d_{im\sigma'}. \quad (1)$$

Here d (f) denotes electrons on Mo (Fe), i labels sites, σ is the spin label, $\ell = 1, 2, 3$ ($\equiv yz, zx, xy$) is the orbital index, and ε is the totally antisymmetric tensor. With $\hat{F} = (\sin\theta\cos\phi, \sin\theta\sin\phi, \cos\theta)$ denoting the Fe moment direction, Pauli exclusion leads to a single spin projection [47] (antiparallel to $\hat{F}$) for electrons on Fe, with $g_\uparrow(j) = \sin(\theta_j/2) e^{-i\phi_j/2}$ and $g_\downarrow(j) = -\cos(\theta_j/2) e^{i\phi_j/2}$. Matrix elements t^{ij} correspond to intraorbital Mo-Fe hoppings t_π, t_δ, while η^{ij} encodes Mo-Mo intraorbital hopping amplitudes t', t'' and interorbital hopping amplitude t_m (see the Supplemental Material for details of hopping processes [62]).

Such a Hamiltonian, with strong SOC and $\chi_{\rm tri} = 0$, has been shown [54] to capture the phenomenology of the bulk Ba_2FeReO_6, quantitatively explaining its band dispersion [55], saturation magnetization [50,56], the spin and orbital polarizations [57], and spin dynamics observed using neutron scattering [58]. For SFMO, our model captures the key energy scales: (i) the implicit strong Hund's coupling on Fe^{3+} (~1 eV, a value typical for $3d$ TM ions [59]), (ii) the Fe-Mo charge transfer energy ($\Delta \sim 0.5$ eV) [43,47], (iii) the nearest-neighbor intraorbital Mo-Fe hopping, which leads to electron itinerancy ($t_\ell^{ij} \sim 0.25$ eV) [43,47], and (iv) the SOC on Mo (we set $\lambda \sim 0.12$ eV) is similar in magnitude to Ru [60,61]. (v) Finally, second neighbor intraorbital and interorbital hoppings ($\eta_{\ell\ell'}^{ij} \sim 0.025$ eV) are weak [43,47,60]; nevertheless, they are important to pin the Fe moment direction, leading to a nonzero ferromagnetic T_c in 2D.

Magnetic ground states.—The ground state of bulk SFMO is a ferrimagnet. In order to explore the magnetic structure of the $\{111\}$ SFMO bilayer, we diagonalize the Hamiltonian equation (1) with $\chi_{\rm tri} = 0$ and compute the ground-state energy for various configurations of Fe moments, including (i) ferromagnetic configurations with different spin orientations, (ii) period-2 stripelike configurations with different spin and stripe orientations, and (iii) random configurations. Figure 2(a) compares these energies per Fe site, plotted in units of $t_\pi = 250$ meV, which is the nearest neighbor Mo-Fe hopping amplitude, showing that the ferromagnetic states have the lowest energy,

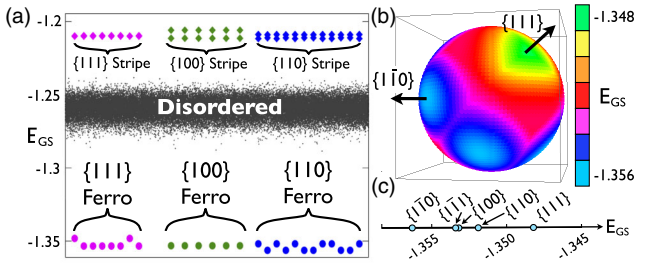

FIG. 2 (color online). (a) Ground-state electronic energy E_{GS} per Fe spin in units of the Mo-Fe hopping $t_\pi = 250$ meV, with $\chi_{\mathrm{tri}} = 0$, shown for different Fe moment configurations including (i) ferromagnetic, (ii) stripelike, and (iii) disordered (random). For ordered states, the label indicates the magnetic moment orientation. (b) E_{GS} for the ferromagnetic states plotted for different orientations of the Fe moments. (c) E_{GS} for the ferromagnetic states for Fe moments along high symmetry directions.

consistent with the kinetic energy lowering due to maximal electronic delocalization. From the energy difference between the ferromagnetic and disordered or stripe configurations, we infer an exchange energy between neighboring Fe moments on the triangular lattice, $J_{FF} \approx 1.5$ meV, close to the bulk 3D value, ≈ 3 meV, estimated from theoretical calculations [47]. The difference stems from the different lattice geometry and the inclusion of SOC.

Unlike previous work, which had Heisenberg symmetry for the magnetism [47], the inclusion of SOC leads to exchange anisotropies, resulting in energy differences between different ferromagnetic orientations of the Fe moments; see Fig. 2(b). With no trigonal distortion, $\chi_{\mathrm{tri}} = 0$, the six $\{1\bar{1}0\}$ orientations with Fe moments lying in the bilayer plane have the lowest energy. As seen from Fig. 2(c), other high symmetry orientations are higher in energy by $\delta E \sim 1$ meV. We have also explored the effect of trigonal distortion on the energy of different ferromagnetic orientations, keeping $\chi_{\mathrm{tri}} \neq 0$. For $\chi_{\mathrm{tri}} < 0$, the energy is minimized by $\vec{L} \| \hat{n}$. This favors the $\{111\}$ orientation of $\vec{L}$, and SOC then forces the spins to also point perpendicular to the bilayer. For $\chi_{\mathrm{tri}} > 0$, it is energetically favorable to have $\vec{L} \perp \hat{n}$, so the $\{1\bar{1}0\}$ orientations remain favorable. We have numerically confirmed these expectations. The combination of SOC and trigonal distortion thus supports a variety of "Ising" or "clock" ferromagnetic ground states.

The broken Heisenberg symmetry induced by exchange anisotropy leads to a nonzero magnetic T_c even in the 2D bilayer. For $\{111\}$ magnetic order, with weak anisotropy energy δE, the Ising transition temperature is implicitly given by $T_c \sim 4\pi J_{FF} S_F^2 / \ln(T_c/\delta E)$ [62]. Using $J_{FF} \approx 1.5$ meV, and computed anisotropy energies across the phase diagram which show $\delta E \sim 0.1$–1 meV, we estimate $T_c \gtrsim 200$ K, lower than $T_c^{\mathrm{bulk}} \sim 400$ K for bulk SFMO but still easily accessible. We next turn to the electronic properties of this SFMO bilayer, focusing on the band topology induced by Fe ferromagnetism.

Chern bands and phase diagram.—We have obtained the magnetic and electronic phase diagram of the SFMO bilayer as a function of the trigonal distortion χ_{tri} and the interorbital hopping t_m. We do this by finding the ferromagnetic orientation of the Fe atoms with the lowest energy, obtained by diagonalizing the Hamiltonian in Eq. (1), and then computing the Chern number of the resulting bands over a finely discretized BZ [66]. Motivated by our finding that the magnetic order and band topology are most sensitive to χ_{tri} and t_m, and recent experiments showing that epitaxial strain can be used to tune the electronic structure in TMO thin films with SOC [68,69], we study the ground states by varying them over a reasonable regime [60,67].

Our calculations yield a rich phase diagram, shown in Fig. 3. We find that the electronic states show the following phases depending on the magnetization direction: (i) normal metal (NM), where the lowest pair of bands overlap in energy and they are both topologically trivial; (ii) a normal insulator (NI) phase, where a full gap opens up between these topologically trivial bands; (iii) a Chern metal (CM), where the lowest pair of bands has nontrivial Chern numbers as indicated, yet overlap in energy, leading to a metallic state with a nonquantized anomalous Hall response; (iv) a $C = \pm 2$ Chern insulator, where weak trigonal distortion opens up a full gap between the two lowest topologically nontrivial bands, leading to a quantized anomalous Hall conductance $\sigma_{xy} = 2e^2/\hbar$ and a pair of chiral edge modes. Figure 4 shows the spectrum of the CI state in a cylinder geometry, depicting a pair of chiral modes at each edge, which cross from the valence to the conduction band. We estimate the bulk gap of the CI state to be $0.03 t_\pi \sim 75$ K.

Emergence of $C = 2$ Chern bands.—Chern bands with $C = 2$ are unusual [70–74] and differ from conventional Landau levels or Hofstadter bands with $C = 1$. How can we understand the emergence of this nontrivial CI? Since the $C = 2$ bands arise for magnetization perpendicular to the bilayer, we begin by studying the phase diagram with Fe moments constrained to point along $\{111\}$. As shown in Fig. 5(a), this leads to a wide swath of the phase diagram where the lowest two bands possess $C = \pm 2$. This lowest

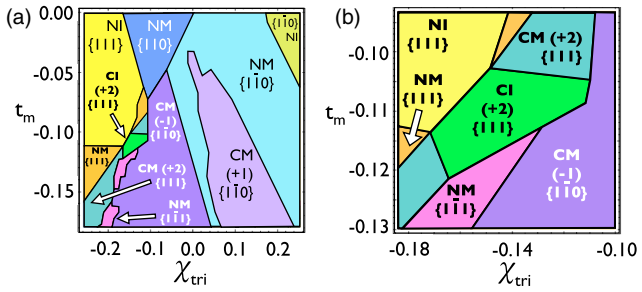

FIG. 3 (color online). (a) Phase diagram of the bilayer as a function of interorbital hybridization t_m and trigonal distortion χ_{tri}. The different phases are Chern metal (CM), Chern insulator (CI), normal metal (NM), and normal insulator (NI). We have also indicated the Fe moment orientations in the different phases and the lowest band Chern number C for nontrivial band topology. (b) Zoomed-in region showing the CI with $C = 2$ and direct NI-CI transition.

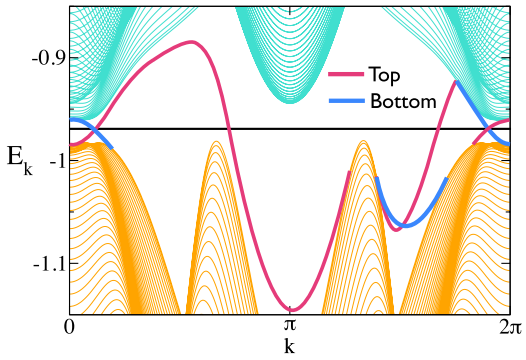

FIG. 4 (color online). Spectrum of the Chern insulator CI in a cylinder geometry, in units of $t_\pi = 250$ meV, against momentum k along the periodic direction. Here, $t_m = -0.11t_\pi$ and $\chi_{\rm tri} = -0.15$. We find a pair of chiral edge modes at each edge, consistent with $C = 2$. The estimated bulk gap is $0.03t_\pi \sim 75$ K.

pair of bands remains separated from the higher bands, allowing one to construct an effective two-band model to gain insight into this physics.

To accomplish this, we note that the predominant role of Fe moments ordered along $\{111\}$ is to produce an exchange field, leading to an effective Zeeman splitting of the spin-orbit coupled $j = 3/2$ states on Mo atoms. The Chern bands arise from the lowest Zeeman-split $j_n = -3/2,\ -1/2$ sublevels, where $j_n = \vec{j}\cdot\hat{n}$ and $\hat{n}\|\{111\}$. Choosing the spin-quantization axis along $\hat{n}$, the Mo wave functions are $|j_n = -3/2\rangle = (1/\sqrt{3})(|yz\rangle + \omega^2|zx\rangle + \omega|xy\rangle)|\downarrow\rangle$ and $|j_n = -1/2\rangle = -(\sqrt{2}/3)(|yz\rangle + |zx\rangle + |xy\rangle)|\downarrow\rangle + \frac{1}{3}(|yz\rangle + \omega^2|zx\rangle + \omega|xy\rangle)|\uparrow\rangle$, where $\omega = e^{i2\pi/3}$. Projecting the full model to these lowest two states (see Supplemental Material for derivation [62]) leads to a two-band triangular lattice model with *complex* interorbital hopping. Near the Γ point, the interorbital hopping takes the form $\sim(k_x + ik_y)^2$; band inversion induced by increasing t_m thus produces a momentum-space Skyrmion with winding number 2, as shown in Fig. 5(b), resulting in the observed $C = 2$ Chern bands. Weak trigonal distortion opens a full gap leading to a CI.

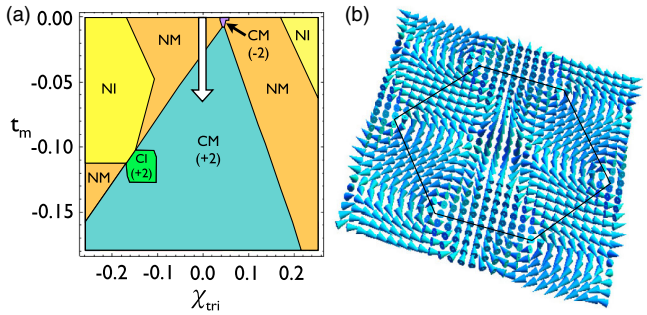

FIG. 5 (color online). (a) Phase diagram with Fe moments along $\{111\}$, showing that the CI state arises within a wide region of $C = 2$ bands. (b) Momentum space Skyrmion with winding number 2 for the CI with $C = 2$. Solid black line denotes hexagonal Brillouin zone.

Remarkably, the phase diagram features a direct NI-CI transition, as seen from Fig. 5(a). This transition is driven by a gap closing at the BZ center, leading to a quadratic band touching with 2π Berry phase; this is protected by C_6 lattice symmetry [75].

Discussion.—We have shown that double perovskite metals can exhibit a variety of ferromagnetic orders and band topologies in a $\{111\}$ bilayer. Such Chern bands in half-metals have also been discussed recently at CrO_2-TiO_2 interfaces [27]. Although the topological phases we have discussed are stable to electron interactions, such interactions are marginally relevant at the NI-CI quadratic band touching transition [75–77]. This leads to a window of a *spontaneous* nematic CI near the CI-NI transition [78]. The broken inversion symmetry in the bilayer will lead to a Rashba interaction; while the topological phases we have uncovered are stable to small Rashba coupling, a strong Rashba interaction will drive spin spirals of Fe moments [21,32]. Further work is then necessary to understand the resulting electronic phases. In future work, we will discuss bilayers of $5d$-based double perovskites such as Ba_2FeReO_6 and Sr_2CrWO_6, which have a $5d^2$ or $5d^1$ configuration of electrons resulting in stronger SOC, which could stabilize robust CI phases.

This research was supported by NSERC of Canada. We acknowledge useful discussions with E. Bergholtz, G. A. Fiete, H. Y. Kee, S. B. Lee, S. Parameswaran, M. Randeria, J. M. Triscone, N. Trivedi, and P. Woodward.

Note added.—Recently, Ref. [79] appeared also discussing QAH effect in {001} oriented double perovskite monolayers.

[1] F. D. M. Haldane, Phys. Rev. Lett. **61**, 2015 (1988).
[2] H. Jiang, Z. Qiao, H. Liu, and Q. Niu, Phys. Rev. B **85**, 045445 (2012).
[3] F. Zhang, C. L. Kane, and E. J. Mele, Phys. Rev. Lett. **110**, 046404 (2013).
[4] F. Zhang, X. Li, J. Feng, C. L. Kane, and E. J. Mele, arXiv:1309.7682.
[5] K. Ohgushi, S. Murakami, and N. Nagaosa, Phys. Rev. B **62**, R6065 (2000).
[6] I. Martin and C. D. Batista, Phys. Rev. Lett. **101**, 156402 (2008).
[7] X. L. Zhang, L. F. Liu, and W. M. Liu, Sci. Rep. **3**, 2908 (2013).
[8] A. R. Wright, Sci. Rep. **3**, 2736 (2013).
[9] J. Ding, Z. Qiao, W. Feng, Y. Yao, and Q. Niu, Phys. Rev. B **84**, 195444 (2011).
[10] T. W. Chen, Z. R. Xiao, D. W. Chiou, and G. Y. Guo, Phys. Rev. B **84**, 165453 (2011).
[11] Z. Qiao, S. A. Yang, W. Feng, W.-K. Tse, J. Ding, Y. Yao, J. Wang, and Q. Niu, Phys. Rev. B **82**, 161414(R) (2010).
[12] W. K. Tse, Z. Qiao, Y. Yao, A. H. MacDonald, and Q. Niu, Phys. Rev. B **83**, 155447 (2011).
[13] R. Nandkishore and L. Levitov, Phys. Rev. B **82**, 115124 (2010).
[14] Cui-Zu Chang *et al.*, Science **340**, 167 (2013).

[15] Y. Ando, J. Phys. Soc. Jpn. **82**, 102001 (2013).
[16] S.-G. Cheng, Europhys. Lett. **105**, 57004 (2014).
[17] A. Ohtomo and H. Y. Hwang, Nature (London) **427**, 423 (2004).
[18] J. Mannhart and D. G. Schlom, Science **327**, 1607 (2010).
[19] H. Y. Hwang, Y. Iwasa, M. Kawasaki, B. Keimer, N. Nagaosa, and Y. Tokura, Nat. Mater. **11**, 103 (2012).
[20] L. Fidkowski, H. C. Jiang, R. M. Lutchyn, and C. Nayak, Phys. Rev. B **87**, 014436 (2013).
[21] S. Banerjee, O. Erten, and M. Randeria, Nat. Phys. **9**, 626 (2013).
[22] D. Xiao, W. Zhu, Y. Ran, N. Nagaosa, and S. Okamoto, Nat. Commun. **2**, 596 (2011).
[23] K. Michaeli, A. C. Potter, and P. A. Lee, Phys. Rev. Lett. **108**, 117003 (2012).
[24] X. Hu, A. Ruegg, and G. A. Fiete, Phys. Rev. B **86**, 235141 (2012).
[25] M. Kargarian, J. Wen, and G. A. Fiete, Phys. Rev. B **83**, 165112 (2011).
[26] J. Wang, B. Lian, H. Zhang, Y. Xu, and S.-C. Zhang, Phys. Rev. Lett. **111**, 136801 (2013).
[27] T.-Y. Cai, X. Li, F. Wang, J. Sheng, J. Feng, and C.-D. Gong, arXiv:1310.2471.
[28] B. J. Yang and Y.-B. Kim, Phys. Rev. B **82**, 085111 (2010).
[29] A. Rüegg, C. Mitra, A. A. Demkov, and G. A. Fiete, Phys. Rev. B **85**, 245131 (2012).
[30] A. Rüegg, C. Mitra, A. A. Demkov, and G. A. Fiete, Phys. Rev. B **88**, 115146 (2013).
[31] R. Chen, S. B. Lee, and L. Balents, Phys. Rev. B **87**, 161119 (2013).
[32] X. Li, W. V. Liu, and L. Balents, Phys. Rev. Lett. **112**, 067202 (2014).
[33] S. Okamoto, Phys. Rev. Lett. **110**, 066403 (2013).
[34] E. Tang, J.-W. Mei, and X.-G. Wen, Phys. Rev. Lett. **106**, 236802 (2011).
[35] N. Regnault and B. A. Bernevig, Phys. Rev. X **1**, 021014 (2011).
[36] T. Neupert, L. Santos, C. Chamon, and C. Mudry, Phys. Rev. Lett. **106**, 236804 (2011).
[37] D. N. Sheng, Z.-C. Gu, Kai Sun, and L. Sheng, Nat. Commun. **2**, 389 (2011).
[38] D. Serrate, J. M. D. Teresa, and M. R. Ibarra, J. Phys. Condens. Matter **19**, 023201 (2007).
[39] M. Gibert, P. Zubko, R. Scherwitzl, J. Iniguez, and J.-M. Triscone, Nat. Mater. **11**, 195 (2012).
[40] B. Gray, H.-N. Lee, J. Liu, J. Chakhalian, and J. W. Freeland, Appl. Phys. Lett. **97**, 013105 (2010).
[41] D. J. Singh and C. H. Park, Phys. Rev. Lett. **100**, 087601 (2008).
[42] K.-I. Kobayashi, T. Kimura, H. Sawada, K. Terakura, and Y. Tokura, Nature (London) **395**, 677 (1998).
[43] D. D. Sarma, P. Mahadevan, T. Saha-Dasgupta, S. Ray, and A. Kumar, Phys. Rev. Lett. **85**, 2549 (2000).
[44] T. Saha-Dasgupta and D. D. Sarma, Phys. Rev. B **64**, 064408 (2001).
[45] G. Jackeli, Phys. Rev. B **68**, 092401 (2003).
[46] K. Phillips, A. Chattopadhyay, and A. J. Millis, Phys. Rev. B **67**, 125119 (2003).
[47] O. Erten, O. N. Meetei, A. Mukherjee, M. Randeria, N. Trivedi, and P. Woodward, Phys. Rev. Lett. **107**, 257201 (2011).
[48] V. Kanchana, G. Vaitheeswaran, M. Alouani, and A. Delin, Phys. Rev. B **75**, 220404 (2007).
[49] A. M. Cook and A. Paramekanti (unpublished).
[50] W. Prellier, V. Smolyaninova, A. Biswas, C. Galley, R. L. Greene, K. Ramesha, and J. Gopalakrishnan, J. Phys. Condens. Matter **12**, 965 (2000).
[51] A. Winkler *et al.*, New J. Phys. **11**, 073047 (2009).
[52] J. B. Philipp *et al.*, Phys. Rev. B **68**, 144431 (2003).
[53] For the Mo $4d^1$ configuration, this trigonal distortion could occur as a spontaneous Jahn-Teller effect.
[54] A. Cook and A. Paramekanti, Phys. Rev. B **88**, 235102 (2013).
[55] B. C. Jeon, C. H. Kim, S. J. Moon, W. S. Choi, H. Jeong, Y. S. Lee, J. Yu, C. J. Won, J. H. Jung, N. Hur *et al.*, J. Phys. Condens. Matter **22**, 345602 (2010).
[56] J. M. D. Teresa, J. M. Michalik, J. Blasco, P. A. Algarabel, M. R. Ibarra, C. Kapusta, and U. Zeitler, Appl. Phys. Lett. **90**, 252514 (2007).
[57] C. Azimonte, J. Cezar, E. Granado, Q. Huang, J. Lynn, J. Campoy, J. Gopalakrishnan, and K. Ramesha, Phys. Rev. Lett. **98**, 017204 (2007).
[58] K. W. Plumb, A. M. Cook, J. P. Clancy, A. I. Kolesnikov, B. C. Jeon, T. W. Noh, A. Paramekanti, and Y.-J. Kim, Phys. Rev. B **87**, 184412 (2013).
[59] P. Fazekas, *Lecture Notes on Electron Correlation and Magnetism* (World Scientific, Singapore 1999).
[60] C. Puetter and H. Y. Kee, Europhys. Lett. **98**, 27010 (2012).
[61] T. Mizokawa, L. Tjeng, G. Sawatzky, G. Ghiringhelli, O. Tjernberg, N. Brookes, H. Fukazawa, S. Nakatsuji, and Y. Maeno, Phys. Rev. Lett. **87**, 077202 (2001).
[62] See Supplemental Material at http://link.aps.org/supplemental/10.1103/PhysRevLett.113.077203, which includes Refs. [63–65], for details of the tight-binding model, magnetic transition temperature, and effective two-band model.
[63] S. Chakravarty, B. I. Halperin, and D. R. Nelson, Phys. Rev. Lett. **60**, 1057 (1988).
[64] D. A. Abanin, S. A. Parameswaran, S. A. Kivelson, and S. L. Sondhi, Phys. Rev. B **82**, 035428 (2010).
[65] P. A. Serena, N. Garcia, and A. Levanyuk, Phys. Rev. B **47**, 5027 (1993).
[66] T. Fukui, Y. Hatsugai, and H. Suzuki, J. Phys. Soc. Jpn. **74**, 1674 (2005).
[67] H. Gretarsson *et al.*, Phys. Rev. Lett. **110**, 076402 (2013).
[68] J. Liu *et al.*, arXiv:1305.1732.
[69] C. Rayan Serrao *et al.*, Phys. Rev. B **87**, 085121 (2013).
[70] F. Wang and Y. Ran, Phys. Rev. B **84**, 241103 (2011).
[71] M. Trescher and E. J. Bergholtz, Phys. Rev. B **86**, 241111 (2012).
[72] S. Yang., Z.-C. Gu, K. Sun, and S. Das Sarma, Phys. Rev. B **86**, 241112 (2012).
[73] F. Zhang, X. Li, X. Feng, C. L. Kane, and E. J. Mele, arXiv:1309.7682.
[74] C. Fang, M. J. Gilbert, and B. A. Bernevig, Phys. Rev. Lett. **112**, 046801 (2014).
[75] K. Sun, H. Yao, E. Fradkin, and S. A. Kivelson, Phys. Rev. Lett. **103**, 046811 (2009).
[76] O. Vafek and K. Yang, Phys. Rev. B **81**, 041401 (2010).
[77] F. Zhang, H. Min, and A. H. MacDonald, Phys. Rev. B **86**, 155128 (2012).
[78] A. M. Cook, C. Hickey, and A. Paramekanti, arXiv:1405.5880.
[79] H. Zhang, H. Huang, K. Haule, and D. Vanderbilt, arXiv:1406.4437.